Meteorol. Z. (Contrib. Atm. Sci.), PrePub DOI 10.1127/metz/2020/1033

Boundary-Layer Meteorology

Spatio-temporal Structure of the Boundary Layer under the Impact of Mountain Waves

Norbert Kalthoff[1*], Bianca Adler[1,2,3] and Inge Bischoff-Gauss[4]

[1]Institute of Meteorology and Climate Research, Karlsruhe Institute of Technology (KIT)
[2]Current affiliation: CIRES, University of Colorado Boulder, Boulder, CO, USA
[3]Current affiliation: NOAA Physical Sciences Laboratory, Boulder, CO, USA
[4]Steinbuch Centre for Computing, Karlsruhe Institute of Technology (KIT), Germany

(Manuscript received February 27, 2020; in revised form June 16, 2020; accepted June 16, 2020)

Abstract

During the Hydrological cycle in the Mediterranean Experiment (HyMeX) in autumn 2012 intensive measurements were conducted in the Tavignano Valley, which extends from the centre to the coast of the island of Corsica. On the investigated day, the atmospheric boundary layer (ABL) in the valley showed a distinctive spatio-temporal variability, which resulted from the interaction and superposition of mesoscale dynamically- and thermally-driven processes and dry convection. Based on the observations, not all of the observed ABL characteristics could be explained and hypotheses on the involved processes were formulated in a previous study. To close the observational gaps and to test the hypotheses, high-resolution simulations with the COSMO (Consortium for Small-scale Modeling) model were now performed. The model was able to reproduce the main ABL characteristics and could hence be used to address the processes affecting the ABL. The main features were: in the upper part of the valley, the stable nocturnal ABL was eroded from top and bottom alike by shear-generated turbulent mixing in the vicinity of a mountain wave and buoyancy- and shear-driven surface-based turbulent mixing, leading to a very abrupt increase of the daytime ABL depth. In the lower part of the valley, the ABL remained rather shallow and was dominated by a superimposed thermally-driven sea breeze and upvalley wind. In the afternoon, the formerly deep ABL in the upper part of the valley rapidly decreased when the combined sea breeze and upvalley wind moved up the valley. While the ABL depth was rather horizontally homogeneous in the lower part of the valley and near the coast, it showed a considerable variability in the valley's upper part on scales of a few kilometres due to the varying dominance of the different processes. The local ABL depth also varied considerably in time depending on which influence dominated, i.e. of surface heating, mountain wave or sea breeze and upvalley wind. As the simulated sea breeze strongly depended on the sea-surface temperature, the results were sensitive to the chosen value in the model.

Keywords: mountain wave, sea breeze, upvalley wind, Corsica, thermally-driven circulation, turbulence, HyMeX, mountain boundary layer

1 Introduction

The structure and depth of the atmospheric boundary layer (ABL) depend on the energy exchange at the surface and meso- and large-scale processes alike (e.g., Stull, 1988; Oke, 1992; Garratt, 1994). While its depth can be spatially quite homogeneous over flat and/or homogeneous surfaces, considerable variations in space and time often occur over heterogeneous terrain (e.g., Steyn and Oke, 1982; Zhong and Doran, 1995). Especially over mountains and in valleys in coastal areas, different mesoscale circulation systems, like sea breezes and slope and valley winds, can interact and superimpose, which results in rather complex ABL conditions (e.g., Kossmann et al., 1998; Kalthoff et al., 1998; Rotach and Zardi, 2007; Steyn et al., 2013; De Wekker and Kossmann, 2015).

*Corresponding author: Norbert Kalthoff, Institute of Meteorology and Climate Research, Karlsruhe Institute of Technology, KIT, Hermann-von-Helmholtz-Platz 1 76344 Eggenstein-Leopoldshafen, Germany, e-mail: norbert.kalthoff@kit.edu

Interactions with the large-scale flow can additionally modify the ABL conditions in mountainous terrain (e.g. Whiteman and Doran, 1993; Jackson et al., 2013; Serafin et al., 2017). This concerns the fields of wind, temperature, humidity and turbulence alike (e.g. Jiang and Doyle, 2008; Mayr and Armi, 2010; Strauss et al., 2016). The types of generated flow phenomena depend on parameters like the strength of the large-scale flow, atmospheric stratification and mountain shape (e.g. Vosper, 2004; Durran, 2015; Smith, 2015).

Due to the impact of the orography, the layer of the atmosphere which undergoes a diurnal cycle is deeper over mountainous terrain than over flat terrain and multilayered structures are often found in valleys with a well-mixed layer in the lower part (Serafin et al., 2018; Khodayar et al., 2008; Bischoff-Gauss et al., 2008). In these cases, the ABL is effected by processes acting on timescales longer than those typical for a convective ABL (O(1 h), e.g., Stull, 1988). To account for the basic differences between ABLs over moun-

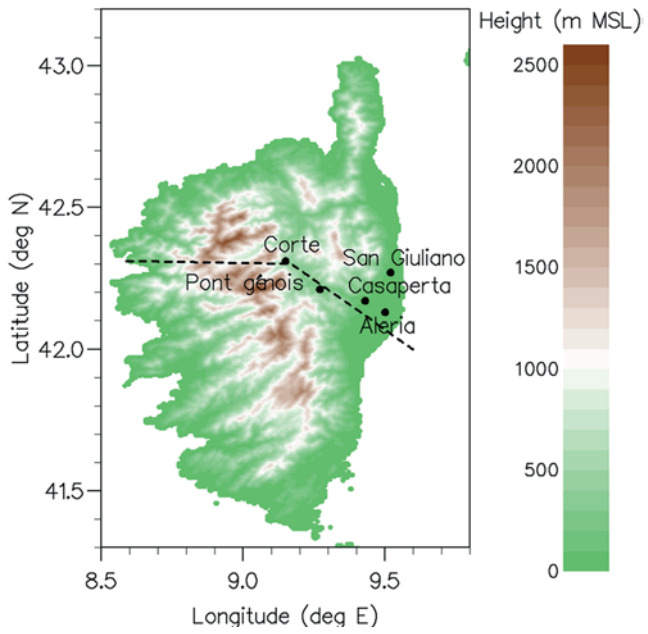

Figure 1: Model orography of the island of Corsica, measurement sites (black dotes) and aircraft flight track (dashed line). Radiosondes were launched at Corte and San Giuliano and surface observations were performed at Corte, Pont génois, Casaperta and Aléria.

tainous regions compared to flat terrain, adequate expressions like alpine boundary layer (alpine BL, Rotach and Zardi, 2007), mountain ABL (Adler, 2014; Adler and Kalthoff, 2016), mountain boundary layer (MoBL, Lehner and Rotach, 2018) have been introduced in recent years. The spatio-temporal variation of the ABL conditions and depth over mountainous terrain and the associated complex exchange of heat, moisture and air pollutants with the free atmosphere (e.g., Kossmann et al., 1999; Kalthoff et al., 2013; Adler et al., 2016; Serafin et al., 2018) are important factors with respect to air quality (Steyn et al., 2013) or the evolution of moist convection (Metzger et al., 2014, Kirshbaum et al., 2018).

During the Hydrological cycle in the Mediterranean Experiment (HyMeX; Drobinski et al., 2014; Ducrocq et al., 2014) in summer and autumn 2012 extensive observations were performed on the island of Corsica in the western Mediterranean Sea (Adler, 2014). The island extends about 180 km in the north-south direction and 80 km in the west-east direction. Its mountain ridge is oriented from the north-northwest to the south-southeast, with its peaks reaching higher than 2000 m above mean sea level (MSL) (Lambert et al., 2011). In the northern part of the island, the Tavignano Valley runs south-east from Corte in the centre of the island towards Aléria on the east coast (Figure 1). Adler and Kalthoff (2014) and Adler et al. (2016) investigated the ABL conditions and the water vapour exchange in the Tavignano Valley and over the island based on measurements. While the focus in these studies was on thermally-driven circulations, Adler and Kalthoff (2016) analysed cases where the ABL conditions were influenced by strong large-scale westerly wind and mountain waves. One of these cases was characterised by the sudden formation of a deep well-mixed ABL associated with warming, drying, wind speed increase, and a turn to large-scale westerly wind direction which occurred nearly simultaneously at two sites in the upper part of the valley. These conditions persisted for several hours before an abrupt cooling, moistening, and turn to south-easterly upvalley wind occurred, first at the site further down and with a time lag of about 2 hours also at the site further up the valley. In the lower part of the valley towards the coast an undisturbed combined upvalley wind and sea-breeze circulation dominated throughout the day. Based on the observational evidence, Adler and Kalthoff (2016) hypothesised that wind shear induced by mountain waves and surface-based convection eroded the stable nocturnal ABL from top and bottom alike. Once the inversion was eroded, the mountain wave approached the surface simultaneously at several locations in the valley explaining the observed concurrency. When the large-scale wind speed decelerated slightly in the afternoon, the combined upvalley wind and sea breeze pushed forward up the valley and first affected the site further down and then the site further up the valley, which explains the time lag.

The aim of this study is now to prove or disprove the observation-based hypotheses of Adler and Kalthoff (2016) and to close observational gaps, which arise as ground-based observations are always point measurements and cannot provide information on the three-dimensional meteorological fields. To this purpose realistic high-resolution COSMO (Consortium for Small-scale Modelling, e.g., Schättler et al., 2008) simulations with 500 m horizontal grid spacing were performed. By combining the observations with the numerical simulations, we aimed to find answers to the questions: (i) what processes caused the strong spatial and temporal variability in ABL characteristics (temperature, humidity, wind, turbulence, depth) along the valley? (ii) How sensitive are the ABL conditions and thermally-driven circulations in the Tavignano Valley on modifications of the sea-surface temperature (SST)?

The paper is structured as follows. Section 2 describes the model setup and the methods used to assess the ABL characteristics. Section 3 gives a short description of the observations and summary of the observed ABL features and assesses the capability of the model to capture them. In Section 4, observations and simulations are combined to generate an integrated view of the ABL evolution and structure. Finally, Section 5 summarises the main findings and concludes.

2 Model setup and method

2.1 Model setup

The COSMO model, version 5.1, was run for this investigation in a one-way nesting mode. The COSMO model

is a fully compressible non-hydrostatic regional weather forecast model (Schättler et al., 2008). We applied the model with a horizontal grid spacing of 500 m nested into a 2.8 km grid. As simulations at 500 m grid spacing are in the "grey zone" (Wyngaard, 2004; Honnert, 2016), the modelled turbulent structures are neither entirely subgrid-scale nor completely resolved. Thus, neither 1-D nor 3-D turbulence parameterisation schemes fit perfectly (Honnert, 2016). Muñoz-Esparza et al. (2016) identified limitations of 1-D turbulence schemes in the context of mountain-wave flows. Nevertheless, simulations in the grey zone make sense (Zhou et al., 2014) because features ranging from sub-mesoscale (ABL heterogeneity) to mesoscale (mountain wave, secondary-circulation systems) can be resolved (e.g. Chow et al., 2006; Barthlott and Hoose, 2015; Adler et al., 2017; Gantner et al., 2017), which is essential for our application. Honnert (2016) stated that turbulence schemes should become tridirectional at around 500 m grid spacing. As there is no definitive recommendation in the literature which parameterisation scheme is best suitable for the simulations in the grey zone over complex terrain, we applied two schemes with 500 m grid spacing: a 3-D turbulence scheme based on the extended Smagorinsky model (Herzog et al., 2002) for turbulent diffusion, as e.g. chosen by Barthlott and Hoose (2015), and additionally a so-called "hybrid" parameterisation scheme, which was introduced by Goger et al. (2018) and accounts for horizontal shear production of *TKE*. In the 3-D parameterisation, the turbulence diffusion coefficients depend on horizontal and vertical grid spacing, stability and turbulent kinetic energy (*TKE*), which is retrieved from a prognostic equation. Unless otherwise indicated, the results shown in the following are based on the 3-D turbulence scheme. For the 2.8 km run the 1-D turbulence scheme described by Raschendorfer (2001) was applied. At both resolutions, the model is convection resolving and convection parameterisation was turned off. A hybrid system with 80 layers up to 22 km with 33 layers below 1.8 km was used. The horizontal differencing is done on a rotated latitude-longitude Arakawa C-grid. In the vertical direction, the generalised terrain-following height-based Gal-Chen coordinate is applied.

The 2.8 km run covers the major part of the Mediterranean Sea (0.9° E–17.55° E, 35.7° N–48.725° N) while the nested 500 m run includes the whole island of Corsica and about 150 km to the west and east (7.265° E–11.155° E, 40.965° N–43.34° N). The orography was taken from the Advanced Spaceborne Thermal Emission and Reflection Radiometer (ASTER) data (e.g. Schmugge et al., 2003). ECMWF-analysis data were taken with a grid spacing of 0.2° for initialisation and boundary conditions of the 2.8 km grid spacing COSMO simulations. Both simulations were initialised on 08 October 2012 at 1200 UTC and run for 36 hours with the boundary conditions being updated every hour. The soil moisture from ECMWF-analysis was modified in the COSMO 2.8 km and 500 m simulations by applying a uniform relative offset of +20 %. This value was determined by adjusting the Bowen ratio, β, at the grid point of Corte to the measured one (which was $\beta \approx 1$). To generate a COSMO simulation which best fits to the observations in terms of the timing of the sea breeze inland propagation, the SST of the original ECMWF-analysis data was modified in the COSMO simulations. This "best result" simulation was achieved by reducing the original SST by 3 °C. The corresponding simulation is denoted as reference run in the following. For the analysis, we used model output on model and z levels and times are given in UTC (CET = UTC + 1). Sunrise was at 0530 UTC and sunset at 16:49 UTC. To prevent boundary effects for the 500 m grid spacing run, the analysis is confined to a smaller area with about 50 km distance to the upstream (western) boundaries. In order to obtain information on the flow, i.e. whether the flow is around the island or over the mountain range, we used the online trajectory module implemented in COSMO (Miltenberger et al., 2013) and started trajectories hourly from 0600 UTC on 09 October onwards at 8.5° E between 41.4° N and 42.7° N with 0.01° increments and from levels between 500 and 3000 m MSL.

2.2 Methods to investigate the ABL characteristics and processes

In the following, we focus on the part of the ABL along the valley between Corte and the coast because the measurements available for model evaluation are restricted to this part of the island. ABL parameters considered relevant for the investigation are temperature, humidity, wind, turbulent kinetic energy (*TKE*) and the ABL depth.

As outlined in Section 1, the conditions in the ABL are influenced by surface fluxes and meso- and large-scale processes. A tendency equation, which describes the growth of a convectively-driven ABL considering the strength of the capping inversion, surface-based buoyancy- and shear-driven turbulence, mean subsidence, and horizontal advection (e.g. Deardorff, 1972; Deardorff, 1974; Driedonks, 1982; Garratt, 1994; Kossmann et al., 1998) can be written as

$$\frac{\partial z_i}{\partial t} = \frac{1}{\gamma}\frac{\partial \Delta_\Theta}{\partial t} + \frac{1}{\gamma}\frac{\overline{(w'\Theta')} - \overline{(w'\Theta')}_{z_i}}{z_i} + w_{z_i} - \left(u_{z_i}\frac{\partial (z_i + z_s)}{\partial x} + v_{z_i}\frac{\partial (z_i + z_s)}{\partial y}\right), \tag{2.1}$$

where z_i denotes the ABL depth, $\frac{\partial \Delta_\Theta}{\partial t}$ is the temporal change of the inversion strength at the ABL top, γ is the vertical potential temperature gradient above the capping inversion, $\overline{(w'\Theta')} = H/(\rho c_p)$ is the kinematic sensible heat flux at the surface, $\overline{(w'\Theta')}_{z_i}$ the one at the ABL top, w_{z_i} is the mean vertical velocity at the ABL top and u_{zi} and v_{zi} are the mean wind velocity components at the height of z_i, z_s is the terrain height. The sensible heat flux at the ABL top is also denoted as entrainment

flux. Driedonks (1982) compared different approaches for calculating the entrainment flux with observations and stated that overall good results are obtained with the formulation

$$-\overline{(w'\Theta')}_{z_i} = a\overline{(w'\Theta')} + b\frac{\Theta u_*^3}{gz_i}, \qquad (2.2)$$

where u_* denotes the friction velocity at the surface. Commonly applied values for the coefficients a and b are $a = 0.2$ (e.g. Stull, 1988) and $b = 5$ (e.g., Driedonks, 1982). The first term on the right-hand side describes the convectively-driven and the second term the mechanically- or shear-driven contribution to entrainment.

Depending on the data available, several algorithms exist for the determination of the ABL depth (e.g., Vogelezang and Holtslag, 1996; Seibert et al., 2000; Rampanelli and Zardi, 2004; Emeis et al., 2008). The Bulk Richardson number, *BRN*, (e.g. Stull, 1988) is often used in models (e.g., Sørensen et al., 1996; Dipankar et al., 2015; Duine and De Wekker, 2017; Coen et al., 2014; Goger et al., 2019). For example, Szintai and Kaufmann (2008) and Seidel et al. (2012) showed that this approach gives reliable measures for convective conditions. The *BRN* is calculated according to:

$$BRN = \frac{gz}{\overline{\Theta}}\frac{\Delta\Theta}{(u^2+v^2)}, \qquad (2.3)$$

where g is the acceleration of gravity, z is the height above the ground, $\overline{\Theta}$ is the mean virtual potential temperature of the layer between z and the surface, u and v are the components of the horizontal wind speed at height z, and $\Delta\Theta$ is the difference of the virtual potential temperature between z and the surface. The level, at which *BRN* reaches a critical number defines the depth of the ABL, z_{BRN}. A value of 0.22 is suggested as critical Richardson number for unstable conditions (Vogelezang and Holtslag, 1996) and of 0.33 for stable conditions (Wetzel, 1982). The *BRN* threshold for stable conditions indicates the top of the portion of a stable ABL in which turbulent mixing due to shear-driven turbulence is likely. The complete depth of a stable ABL is defined as the layer with a strong positive potential temperature gradient (e.g. Mahrt, 1981) and is usually deeper than z_{BRN}.

Note that the z_i-tendency equation (Eq. (2.1)) does not consider e.g. processes like interactions of the large-scale flow with an ABL or shear-induced turbulent mixing caused by mesoscale phenomena and their superposition, like mountain wave, sea breeze, slope and valley winds (e.g., Rotach et al., 2008; Strauss et al., 2016), while the z_{BRN} detection diagnoses the result of all processes, which impact the temperature and wind profiles (Eq. (2.3)). The *BRN*-based determination of an ABL depth thus determines the top of a layer adjacent to the surface which is likely to be mixed, i.e. z_{BRN} does not necessarily coincide with the top of the MoBL, as the MoBL may encompass multiple layers due to the influence of the terrain. That means, the comparison of the detected z_{BRN} value with the predicted value of z_i after Eq. (2.1) indicates whether significant meso-, large-scale or upper-layer processes were involved in the ABL evolution. We used z_{BRN} from COSMO model output and calculated it from observation data and interpret z_{BRN} as ABL depth in the following.

3 Observed and simulated conditions along the Tavignano Valley

During the HyMeX field campaign, measurements were conducted with the KITcube (Kalthoff et al., 2013) on the island of Corsica in autumn 2012. Measurement systems were deployed in the Tavignano Valley at Corte (370 m MSL), Pont génois (185 m MSL), Casaperta (50 m MSL) and on the east coast at Aléria (40 m MSL) and San Giuliano (40 m MSL) (Figure 1). For this investigation we used cloud radar, radiosonde data and near-surface mean and turbulence observations from Corte, near-surface mean and turbulence observations from Pont génois, Casaperta and Aléria and radiosonde data from San Giuliano. For a detailed description of all observation systems and measured data we refer to Adler (2014) and Adler and Kalthoff (2016).

On the investigated day (9 October 2012), the island of Corsica was located in the transition zone between a trough over the Mediterranean and a ridge centred over France and Spain (Adler and Kalthoff, 2016). Associated with this, a strong west north-westerly flow of approximately 15 m s^{-1} prevailed in the mid-troposphere upstream of Corsica as evident from ECMWF analysis data (not shown). These data also indicate that a well-mixed maritime ABL of about 400 m depth established over the sea while the atmosphere above the maritime ABL was stably stratified ($\frac{\Delta\Theta}{\Delta z} \approx 4$ K km^{-1}). Within this stably stratified layer (between 2.5 and 3.5 km MSL), mountain waves were observed over the island (Figure 2). The observed mountain waves with wavelengths of 15 to 20 km and considerable vertical velocities (up to 5 m s^{-1}) were well reproduced by the COSMO model (Figure 2).

Based on the radiosoundings performed at Corte and San Giuliano and the near-surface observations at Pont génois, Casaperta, and Aléria, the atmospheric conditions on 9 October can be divided into three time phases (Adler and Kalthoff, 2016):

Phase I (<0800 UTC): At Corte at 0500 UTC, the *BRN*-based ABL-depth estimation gives $z_{BRN} = 33$ m above ground level (AGL), i.e. about 400 m MSL. The height of the nocturnal stable ABL reached up to 700 m AGL (≙ 1070 m MSL), as indicated by a considerable reduction of the potential temperature gradient from about 1.2×10^{-2} to 0.2×10^{-2} K m^{-1} at that level (Figure 3a). This means that mechanically-induced turbulent mixing occurred only in the lowest 5 % of the stable ABL. In the stable ABL, the wind was weak

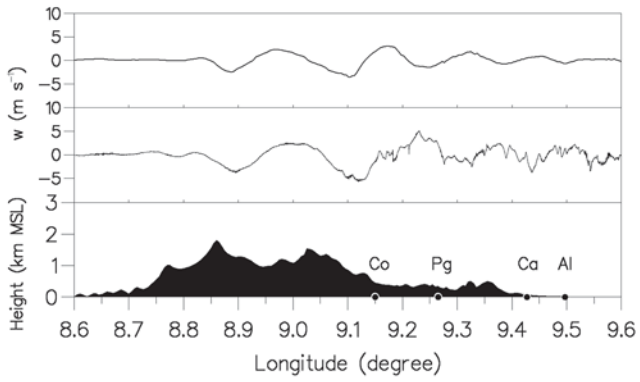

Figure 2: Vertical wind speed from simulations (top) and aircraft observations (middle) as well as orography (bottom) along the flight track (see Figure 1). Observations and simulations are at around 3000 m MSL and 1130 UTC. The positions of Corte (Co), Pont génois (Pg), Casaperta (Ca) and Aléria (Al) are indicated.

coming from varying directions. At the top of the stable ABL, the wind turned to west north-westerly direction and increased strongly with height leading to strong wind shear. The wind speed increased further with height reaching about 20 m s^{-1} at the mountain crests at around 2000 m MSL. At San Giuliano at 0500 UTC, an ABL depth of $z_{BRN} = 30$ m AGL ($\hat{=}$ 70 m MSL) was found, while the nocturnal stable ABL reached up to 250 m AGL (290 m MSL). In the whole stable ABL, weak winds prevailed, while west north-westerly winds that increased in strength with altitude existed in the moderately stable stratified layers above (Figure 3c). The corresponding near-surface conditions at the measurement sites along the valley are shown in Figure 4a. Due to increasing net radiation and an associated growth of the surface sensible heat flux (both not shown), the temperature rose continuously at all sites after around 0600 UTC. In agreement with the radiosonde profile (Figure 3a), the stations measured low wind speed (≈ 1 m s^{-1}) and low *TKE* (< 1 m^2 s^2). In the upper part of the valley (Corte and Pont génois), the wind blew from changing directions while north-westerly wind dominated at the stations closer to the coastline (Casaperta, Aléria). The main nocturnal ABL characteristics at Corte and San Giuliano were quite well reproduced by the model simulations (Figures 3b, d and 4b), i.e. low z_{BRN} heights, much deeper stable ABLs with weak winds and low turbulence and strong large-scale wind above. However, some differences can also be found: e.g., the model does not reproduce the low temperature at Pont génois or the high specific humidity at Corte.

Phase II (0800 to 1300 UTC at Pont génois and 0800 to 1430 UTC at Corte): At Corte, the 700 m deep stable ABL was already eroded at about 0800 UTC and a deep ABL had established with $z_{BRN} = 800$ m AGL ($\hat{=}$ 1170 m MSL) and westerly wind existed all the way down to the surface (Figure 3a). Until 1000 UTC, the ABL grew further to $z_{BRN} = 1250$ m ($\hat{=}$ 1620 m MSL). The evolution of the deep ABL and onset of westerly winds were reproduced adequately by the model. At the same time, considerable downward motion set in in this layer (Figure 5a), which also occurred in the model simulation (Figure 5b). Again, local differences exist: e.g., the simulated wind speed at the surface at Corte is higher than the observed one and at all surface stations *TKE* is systematically underestimated (Figure 4). Both differences also occur when applying the hybrid parameterisation scheme of Goger et al. (2018) (not shown). Zhong and Chow (2013) and Goger et al. (2018) also found an underestimation of *TKE* by models over complex terrain. In our observations, *TKE* is dominated by the horizontal variances, $\overline{u'^2}$ and $\overline{v'^2}$ (not shown). Their values are about four times higher than the vertical variance, $\overline{w'^2}$. Thus, it can be expected that the underestimation of *TKE* in the model is caused by its underestimation of $\overline{u'^2}$ and $\overline{v'^2}$.

At San Giuliano at 0800 UTC, the observations show an ABL depth of $z_{BRN} = 375$ m AGL ($\hat{=}$ 415 m MSL) and a weak easterly wind established within the ABL (Figure 3c), which indicates that the sea breeze had reached the station. The observed slight increase of z_{BRN} between 0600 and 0800 UTC was also simulated by the model (Figure 3d). The near-surface conditions along the valley and at the coast were as follows: at Corte and Pont génois, phase II began with a rapid increase in temperature, a decrease in humidity, a change in wind direction to westerly and an increase of wind speed, u_* (not shown) and *TKE* (Figure 4a). After these rapid changes, the conditions remained quite constant for the rest of phase II. More towards the coast, i.e. in Casaperta and Aléria, however, the temperature and specific humidity increased further and the wind, gradually turning to easterly wind direction, indicates that an up-valley/sea-breeze circulation has started to form. Wind speed, and *TKE* were much lower than at Corte and Pont génois (Figure 4a). While the overall simulated near-surface conditions fit with the observations at Corte, Casaperta and Aléria, the onset of westerly wind and decrease of humidity were somewhat delayed in the simulations at Pont génois (Figure 4b). Possible reasons for this discrepancy are discussed in Section 4.

Phase III (after 1300 UTC at Pont génois and after 1430 UTC at Corte): At both sites, this period was initiated by a change from westerly to easterly wind, by a considerable rise of specific humidity (from approximately 8.5 to 12 g kg^{-1}) and a reduction of turbulence (Figure 4a). These changes were first observed at Pont génois and about two hours later at Corte, which again is reproduced by the model (Figure 4b). As visible in the radiosonde profiles and cloud-radar observations, z_{BRN} decreased considerably at Corte within this phase (Figure 3a) and upward motion of about 1 m s^{-1} up to at least 2000 m MSL occurred (Figure 5a). This observed simultaneous decrease of z_{BRN} and onset of significant upward motion is also visible in the model simulations (Figures 3b and 5b). In the lower part of the valley and at the coast, the ABL conditions did not change much until the late evening as evident from both the observations

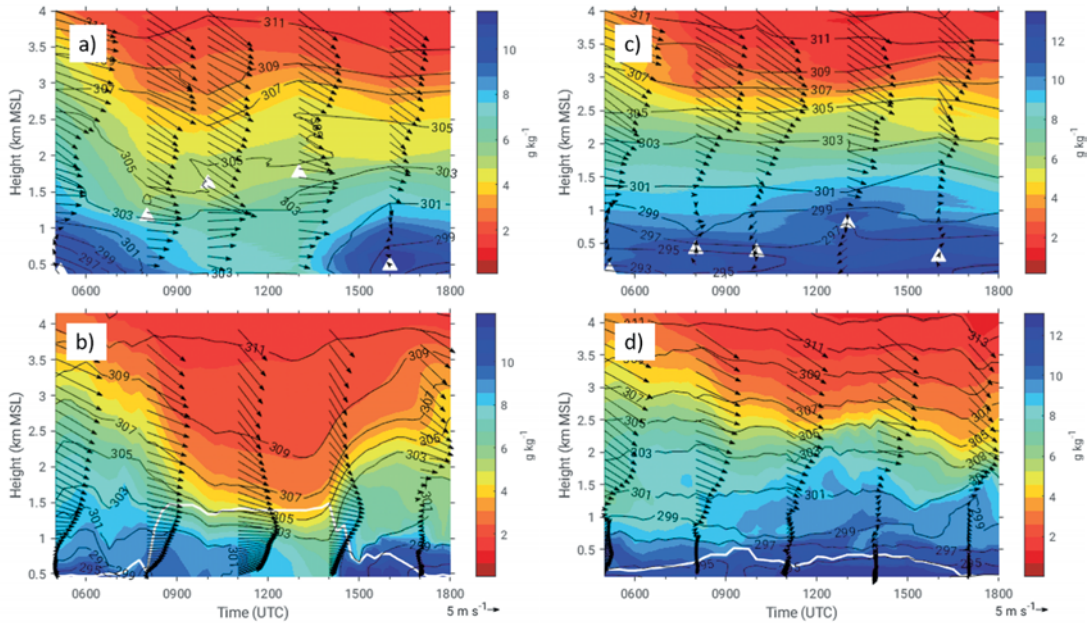

Figure 3: Specific humidity (colour-coded), potential temperature (black isolines) and horizontal wind (arrows) measured with radiosondes (a) and simulated (b) at Corte and measured (c) and simulated (d) at San Giuliano. In (a) and (c), z_{BRN} is indicated by triangles and in (b) and (d) by solid white lines.

and simulations (Figures 3c,d and 4a, b). At Casaperta, a weak west north-westerly wind of $\approx 1\,\mathrm{m\,s^{-1}}$ was already observed after 1600 UTC, which was not simulated by the model.

Overall, the main features of the observed ABL properties relevant for this investigation were adequately captured by the COSMO model. These are the nearly simultaneous erosion of the nocturnal surface inversion at Corte and Pont génois (end of phase I); the strong and abrupt increase of a well-mixed ABL at Corte; the subsequent, considerable subsidence extending over the entire ABL for several hours (phase II); and the time-shifted change of the ABL conditions at Corte and Pont génois in the afternoon (onset of phase III), accompanied by a remarkable drop of the ABL depth and strong upward motion in and above the ABL, which lasted for more than one hour.

4 Spatio-temporal ABL variability

4.1 Processes determining the ABL conditions at the different sites

Justified by the satisfactory agreement between the observations and model simulations concerning the main ABL characteristics, we now combine both sources of information to develop an overall view of the spatio-temporal ABL evolution and the involved processes in the Tavignano Valley.

4.1.1 Transition from phase I to phase II

To estimate the contribution of surface-based buoyancy and wind shear on the ABL growth rate at Corte during the transition from phase I to phase II, we applied Eq. (2.1) using observational data. The values used to calculate the z_i tendency are summarised in Table 1. Under these conditions, z_i at the end of phase I (0800 UTC) would have reached up to about $z_i \approx 290\,\mathrm{m}$ AGL ($\hat{\approx} 660\,\mathrm{m}$ MSL, Tab. 1). This is only 36 % of what was observed ($z_{BRN} \approx 800\,\mathrm{m}$ AGL ($\hat{\approx} 1170\,\mathrm{m}$ MSL), Figure 3a), i.e. the value of z_{BRN} indicates that the stable ABL of around 700 m depth was already eroded. If we compare the contribution from buoyancy (surface flux and entrainment flux) with the one from shear-driven entrainment on the total z_i growth (Eqs. (2.1) and (2.2)), buoyancy contributed about 70 % and shear about 30 % to the growth of z_i at the end of the transition period (0700 to 0800 UTC) (Tab. 1).

Integration of Eq. (2.1) further in time from 0800 to 0900 UTC results in an additional z_i increase of 308 m so that $z_i(0900\ \mathrm{UTC}) \approx 600\,\mathrm{m}$ AGL ($\approx 970\,\mathrm{m}$ MSL, Tab. 1). A linear interpolation of z_{BRN} results in $z_{BRN}(0900\ \mathrm{UTC}) \approx 1030\,\mathrm{m}$ AGL ($\approx 1400\,\mathrm{m}$ MSL, Figure 3), i.e. a ratio of $z_i/z_{BRN} \approx 60\,\%$. According to Eq. (2.1), the dominant contribution to z_i growth during this period is shear-driven entrainment ($\approx 84\,\%$) while buoyancy only accounts for about 16 % (Tab. 1). The comparison of the estimated z_i with z_{BRN} shows that the processes considered in Eq. (2.1) are not sufficient to explain the changes of the ABL conditions during the transition period from phase I to phase II. That means, additional processes must have been active during this period, which are not represented in the simple tendency equation.

More insight into the processes leading to the abrupt transition from phase I to II is gained from the model simulation. At 0700 UTC, there is still a stable ABL present at Corte (Figures 3b and 6a). However, shear-

Table 1: Values used for the estimation of $z_i(t)$ with Eq. (2.1). Values were derived from the energy balance station and radiosonde at Corte for the indicated time intervals; $z_i(t_0)$ and $z_i(t_1)$ denote the ABL heights at the beginning respectively end of the corresponding time interval. z_i(0500 UTC) was calculated with Eq. (2.3) from the radiosonde profiles. The convective and mechanical entrainment fluxes were calculated with Eq. (2.2).

	0500–0600 UTC	0600–0700 UTC	0700–0800 UTC	0800–0900 UTC
u_* (m s^{-1})	0.11	0.17	0.3	0.84
$\overline{\Theta}$ (K)	291	291	291	294
γ, (K m^{-1})	1.5×10^{-2}	1.5×10^{-2}	1.5×10^{-2}	1.5×10^{-2}
$\overline{w'\Theta'}$ (K m s^{-1})	0.0	0.011	0.049	0.05
$\overline{w'\Theta'}_{z_i,\ convective}$ (K m s^{-1})	0.0	0.002	0.01	0.01
$\overline{w'\Theta'}_{z_i,\ mechanical}$ (K m s^{-1})	0.006	0.01	0.027	0.309
$z_i(t_0)$ (m AGL/MSL)	33/403	76/446	148/518	287/657
$\frac{\partial z_i}{\partial t}$ (m h^{-1})	43	72	140	308
$z_i(t_1)$ (m AGL/MSL)	76/446	148/518	287/657	596/966

generated turbulence is already active at the top of the stable layer (Figure 6a), which means that the stable ABL is eroded simultaneously from the bottom and top by surface-based buoyancy- and shear-driven turbulence. This elevated shear layer is related to the mountain wave which already penetrated into the valley west of Corte at 0700 UTC (not shown). Due to the increasing surface sensible heat flux and continuous shear-driven turbulence, the stable ABL was completely eroded at 0800 UTC and the mountain wave penetrated down to the valley floor (Figures 6a and 7a, b). This was associated with downward mixing of momentum and dry air, which explains the decrease of specific humidity, the onset of strong westerly wind accompanied by enhanced turbulence near the surface (Figure 4) and the abrupt rise of the ABL depth at Corte (Figure 3). As Corte is within the downward directed branch of the mountain wave (Figure 7a, b), this also explains the presence of strong downward motion lasting for several hours (Figure 5a, b) and confirms the hypotheses formulated by Adler and Kalthoff (2016). Based on the model results, we can thus exclude that the strong and persistent downward motion was caused by the subsiding branch of a thermally-driven cross-valley wind circulation, which can also lead to subsidence in the centre of a valley (e.g., Atkinson, 1981; Whiteman, 2000). According to the simulations, at least in some areas in the lower part of the valley a stable ABL still existed at this time as visible from the isentropes (Figure 7a). To study the sensitivity of the ABL behaviour on the turbulence parameterisation scheme, results from the hybrid scheme (Goger et al., 2018) are shown in Figure 6b. While the ABL conditions during phase II and III were quite similar, some differences concerning the transition from phase I to II can be found. The stable layer was already eroded after 0630 UTC, i.e. about 1 h earlier than in the run with the 3-D turbulence scheme, and the ABL reached up to around 1000 m MSL between 0700 and 0800 UTC.

Comparing the interaction of the mountain wave with the ABL in the valley with previous investigations reveals both similarities and differences. As simulated by Jiang and Doyle (2008) and observed by Serafin et al. (2017) and Haid et al. (2020), cold pools in the valley inhibit the propagation of a mountain wave to reach the valley floor. During periods with stable surface layers or cold pools, wave-generated turbulent regions are located on top of them (Strauss et al., 2016; Haid et al., 2020). This very much resembles the conditions during our phase I. Whiteman and Doran (1993); Serafin et al. (2018) and Mayr and Armi (2010) found that the impact of the overlying large-scale flow on the in-valley flow increases with the strength of the large-scale flow, e.g. mountain wave, and reduction of atmospheric stability. Differences can be found between our observations and previous results for the period when the mountain wave reaches the valley floor. While e.g. Mayr and Armi (2010) and Jiang and Doyle (2008) reported that in the Owens Valley this only occurred when the surface heat flux reaches a maximum or the ABL top reached the top of the surrounding mountain crests, which is usually in the early afternoon, in our case the downward penetration of the mountain wave occurs as soon as the nocturnal ABL was eroded.

Despite the slight temporal delay in the change of the near-surface conditions at Pont génois in the simulation compared to the observations (Figure 4a, b), the simulation nevertheless can be used to explain the similar temporal behavior observed at both sites. The trajectories shown in Figure 8a were started at 1800 m MSL west of Corsica at 0800 UTC. Assuming that the parcels travel with the mean upstream wind speed of 15 m s^{-1}, they pass the mountain crest about 1 h later. The axis of the mountain wave is roughly aligned with the orientation of the main mountain crest on the island of Corsica, i.e. it is oriented from northwest to southeast. The part of the wave with upward motion (indicated by a larger height level of the trajectories) is situated upwind and over the mountain crest and the one with downward motion (indicated by a lower height level of the trajectories) downwind of the crest. On the downwind side of the mountain crest, the wave penetrated deep into the valley at several locations as indicated by the low height levels of the trajectories. This explains why westerly wind

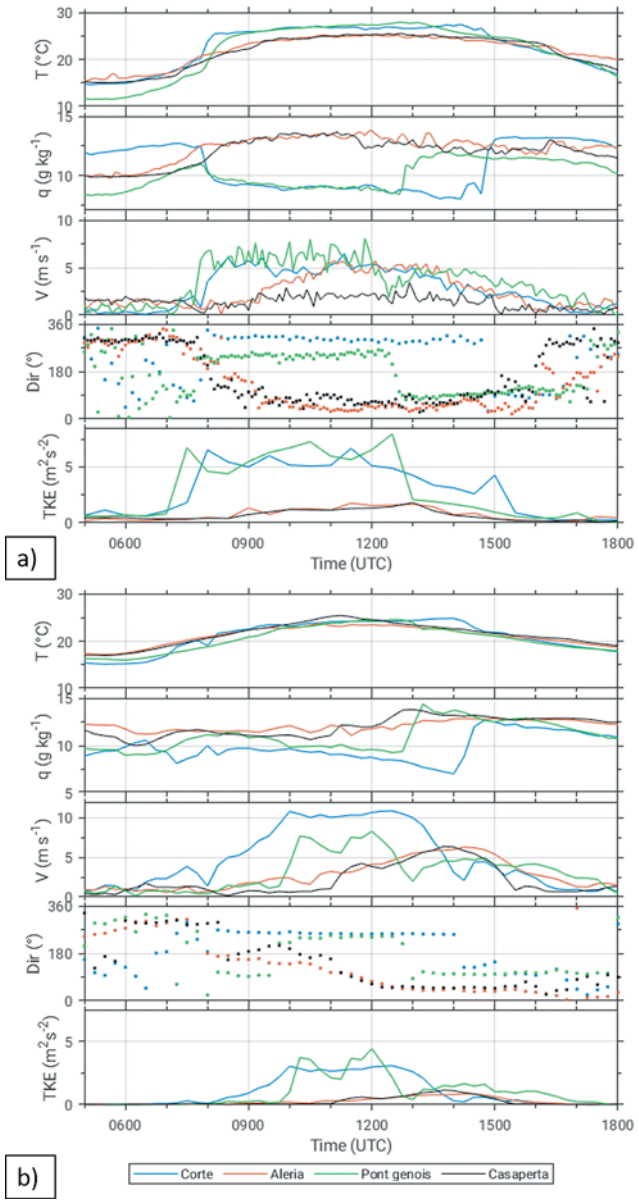

Figure 4: Near-surface temperature, T, specific humidity, q, horizontal wind speed, V, wind direction, Dir, and turbulent kinetic energy, TKE as given from observations (a) and simulations (b) at the designated stations. The time stamps of the observed parameters mark the end of the 10-min intervals (30-min interval for TKE) while the simulations are instantaneous values every 15 min. The positions of the stations are marked in Figure 1.

and dry air masses are simulated on the slopes downwind and at several sites in the western parts of the valley floor at and after 0800 UTC (Figure 8b). In particular around Pont génois, the conditions are very sensitive to the selected grid point: at 0800 UTC, westerly wind and low humidity are simulated about 3 km south-west of Pont génois (which indicates that the wave reached down to the ground in this area), while the exact position of Pont génois is not affected by the mountain wave until about one hour later (Figure 4b). At 0800 UTC and later, the surface stations closer to the coast (San Giuliano and Aléria) are not influenced by mountain waves.

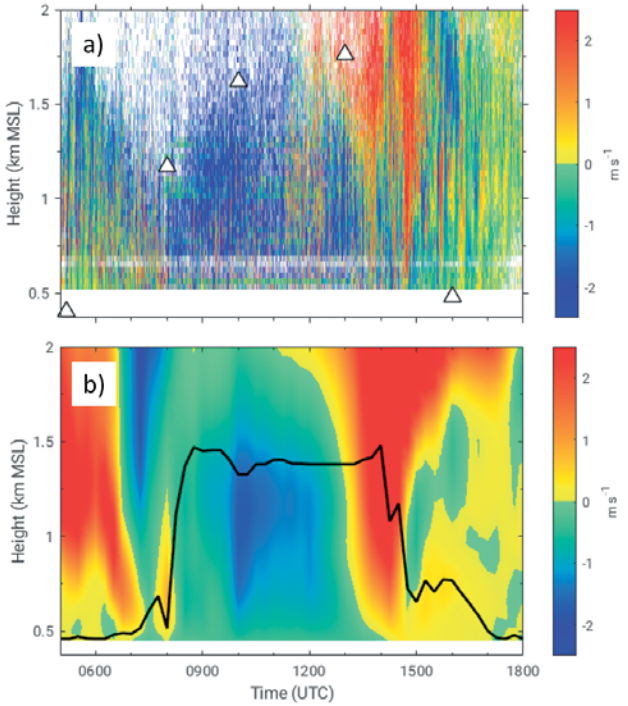

Figure 5: Vertical wind speed measured with the cloud radar (10 s, colour coded) (a) and simulated (15 min, colour coded) (b) for Corte. In (a), z_{BRN} is indicated by triangles and in (b) by a solid black line.

These sites were under the influence of the sea breeze, indicated by moist air and easterly winds (Figures 3, 4 and 8b). The sea-breeze layer with a depth of about 350 to 400 m (≙ 400 to 450 m MSL) remained present throughout the entire day, as evident in Figure 3c, d.

4.1.2 Phase III

The beginning of phase III is indicated by a strong decrease of the ABL depth, a reversal in wind direction and an increase of humidity, which happened first in the area of Pont génois around 1300 UTC (Figure 4). The simulations clearly indicate that this is due to the arrival of the sea-breeze front (Figure 8c). The conditions in the valley around Pont génois are highly heterogeneous in space: the sea breeze was present in the north-eastern part of the valley, while the south-western part was still under influence of the mountain wave at that time. About 1.5 h later, the maritime airmass also reached Corte (Figure 8d). The ABL depth within the maritime air mass was some hundred meters only (Figure 7c). The arrival of this air mass at Corte was accompanied by considerable upward motion (Figure 5a, b). The upward motion in the ABL occurred when the westerly wind component of the mountain wave and the easterly wind component of the sea breeze converged (Figure 7c). The arrival of the sea breeze also led to a stabilisation of the valley atmosphere so that the mountain wave lifted off and retreated toward the western slope (Figure 7c). Thereby, the layers above the ABL came under the influence of the ascending branch of the mountain wave (compare

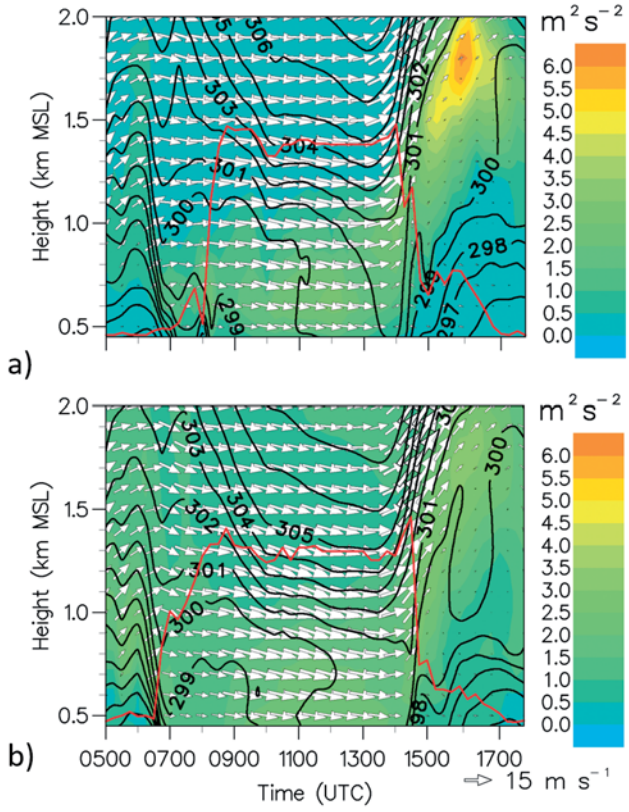

Figure 6: Simulated *TKE* (colour coded), potential temperature (isolines), z_{BRN} (solid red line), and u,w-wind vector (the w-component is multiplied by a factor of 3) at Corte based on the 3-D turbulence parameterisation (a) and hybrid scheme (b). For details see Section 2.

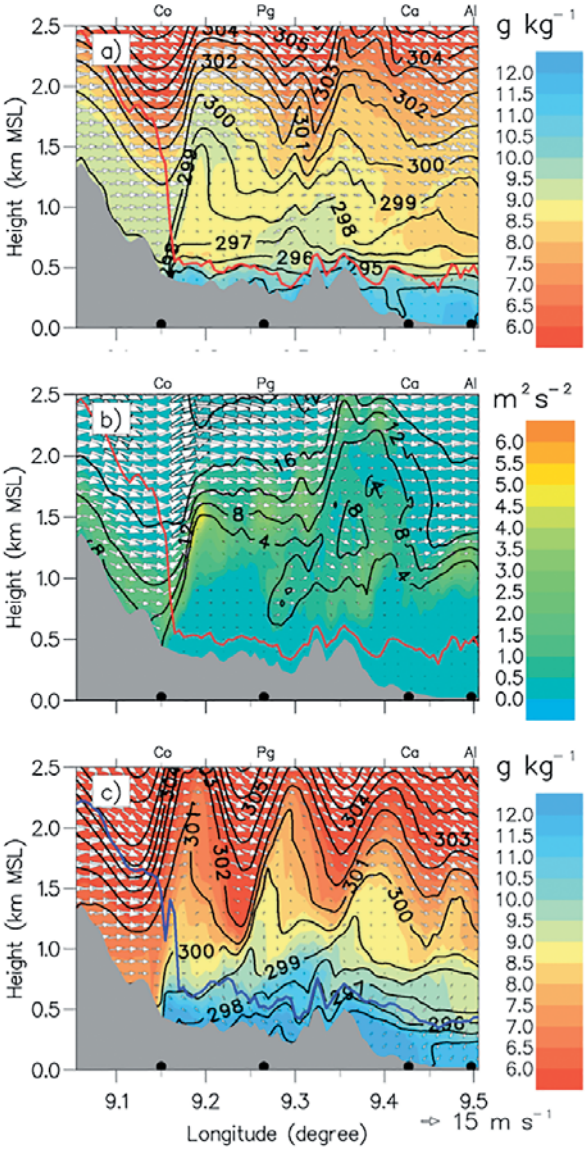

Figure 7: Simulated specific humidity (colour coded), potential temperature (isolines), and u,v-wind vector (arrows) at 0830 UTC (a) and 1430 UTC (c). *TKE* (colour coded), absolute value of horizontal wind speed (isolines), and u,w-wind vector (arrows, the w-component is multiplied by a factor of 3) at 0830 UTC. In (a) and (b) z_{BRN} is indicated as solid red line and as blue line in (c). The cross sections are along the flight track (see Figure 1). The positions of Corte (Co), Pont génois (Pg), Casaperta (Ca) and Aléria (Al) are marked as black dots.

Figure 7a and c), indicated by the strong upward motion above the ABL (Figure 5). The sensitivity experiments (see Section 4.2.3), where the SSTs are modified lead to a time shift of the sea breeze and are accompanied by a corresponding time shift of the upward motion in and above the ABL (not shown). As the large-scale flow is the same in all three sensitivity runs, we conclude that the decisive factor for the observed changes of the ABL conditions is the arrival of the sea breeze and not the large-scale flow reduction of about 20 % between 0800 and 1400 UTC at 5 km MSL. A lifting of a mountain wave due to the evolution of a stable stratification was also observed and simulated by Jiang and Doyle (2008). However, in their case the stable stratification was caused by radiative cooling in the evening instead of cold air advection. After the maritime air mass had filled up the entire valley around Corte, the upward motion was no longer present in the ABL – neither in the observations nor in the simulations (Figure 5a, b). The observed and simulated abrupt decrease of the ABL depth in Corte at 1430 UTC (Figures 3a, b and 6) can be explained by a negative contribution of horizontal advection to the z_i-tendency, as a large spatial z_i-gradient existed along the valley axis related to the approaching sea breeze (Figure 7c). The simulation confirms the hypotheses of Adler and Kalthoff (2016) on the decisive role of the superimposed upvalley wind and sea breeze circulation for the ending of the period, during which the mountain wave dominated the ABL conditions.

4.2 Spatio-temporal variability and sensitivity of the ABL depth

It is evident from the observations and simulations that the ABL in the Tavignano Valley exhibited a high temporal and spatial variability on this particular day, and it was demonstrated in the previous section that driv-

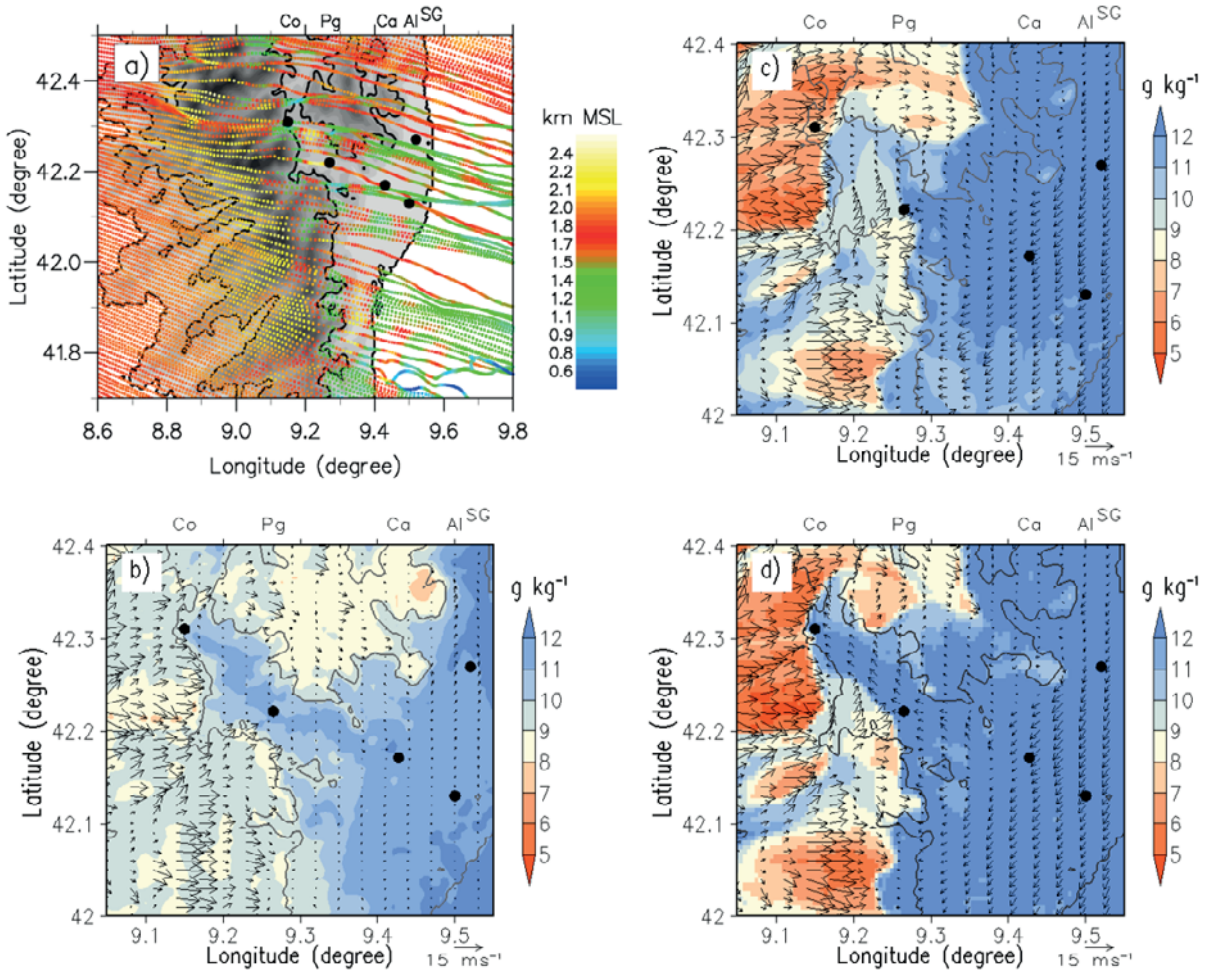

Figure 8: Simulated trajectories with corresponding height levels (colour coded) started at 1800 m AGL at 0800 UTC to the west of the island of Corsica (a) and horizontal wind speed at 10 m AGL (arrows) and specific humidity at 2 m AGL (colour coded) at 0800 UTC (b), 1300 UTC (c) and 1430 UTC (d). The 600 m-contour line is highlighted (black solid line). Dots mark the measurement stations Corte (Co), Pont génois (Pg), Casaperta (Ca), Aléria (Al) and San Giuliano (SG) (see Figure 1).

ing factors are mountain waves, buoyancy- and shear-driven turbulence and the combined effect of the valley wind and sea breeze circulation. We will now use the simulations to investigate (i) the small-scale variability (meso-γ scale), which also reflects the representativity of an individual grid point with respect to the conditions in its surrounding, (ii) the spatio-temporal variability of the ABL depth along the floor of the valley (terrain heights < 600 m MSL), i.e. variability on the meso-β scale, and (iii) the impact of the SST on ABL evolution and distribution.

4.2.1 Small-scale variability of the ABL depth

Figure 9 shows the diurnal cycles of the mean ABL depth, $\overline{z_{BRN}}$, and its standard deviations, $\sigma_{z_{BRN}}$, calculated from an area consisting of 7×7 model grid points ($\hat{=} 12.25\,\mathrm{km}^2$) centred on the individual sites. The ABL depths at the grid points closest to the individual sites are added. The diurnal cycles of the mean ABL depth in the valley (Corte, Pont génois, Casaperta, Figure 9a) differ considerably in time and amplitude ($\overline{z_{BRN}}$ reaches up to 1150 m AGL at Casaperta), while their values at the coast (San Giuliano, Aléria, Figure 9b) are much lower ($\overline{z_{BRN}} < 450$ AGL) and more consistent in time. The ABL depths at the valley sites have much larger $\sigma_{z_{BRN}}$ values than at the coastal sites, e.g. in the surrounding of Pont génois at around noon. This also indicates that the representativity of ABL depths of individual sites in the valley is quite limited. Individual ABL depths do not even fall into the range of $\overline{z_{BRN}} \pm \sigma_{z_{BRN}}$, e.g. at Corte during the two transition phases at the beginning and end of phase II and at Pont génois at around noontime. This higher spatial heterogeneity of z_{BRN} in the valley than along the coast is also reflected in Figure 10a, where the spatial z_{BRN} distribution at 1100 UTC is depicted. This time is chosen because a considerable spatial variability of z_{BRN} was simulated, e.g. z_{BRN} varies from a few hundred meters to about 1500 m AGL (Figure 9). The reasons for the variability of the ABL depth is investigated in the next section.

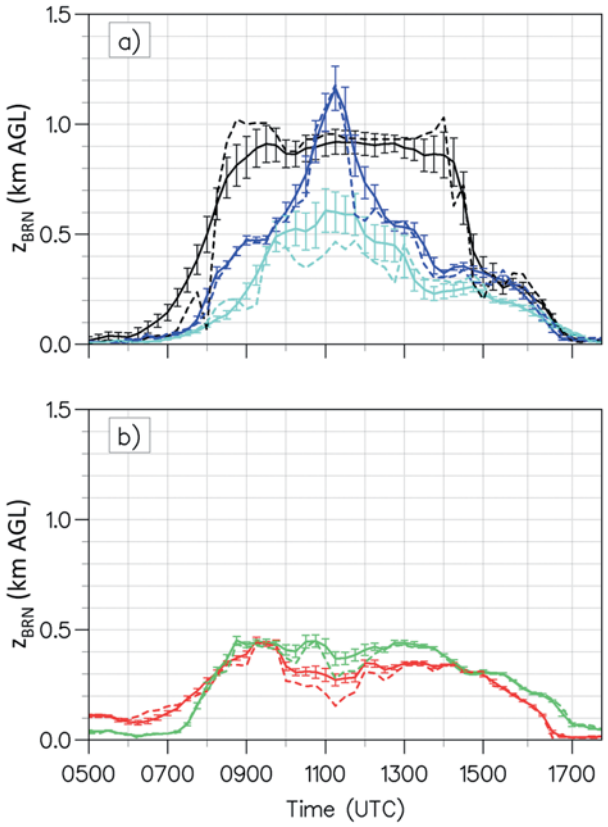

Figure 9: Simulated mean ABL depths, $\overline{z_{BRN}}$, (solid lines), their standard deviations, $\sigma_{z_{BRN}}$, (error bars) and the individual ABL depths (dashed lines) for Corte (black), Pont génois (light blue) and Casaperta (dark blue) (a) and San Giuliano (red) and Aléria (green) (b). The mean and $\sigma_{z_{BRNi}}$ values are calculated from an area consisting of 7×7 model grid points centred on the individual sites.

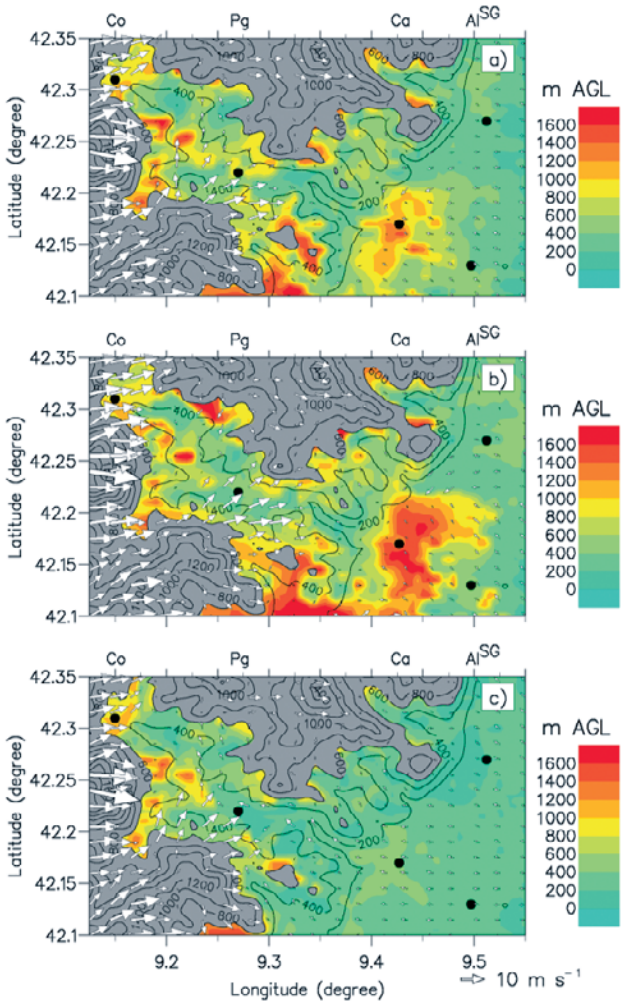

Figure 10: Simulated spatial distribution of z_{BRN} (colour-coded) in the valley (terrain heights < 600 m MSL), terrain heights (black isolines) and horizontal wind at 10 m AGL (arrows) at 1100 UTC from the reference run (a), for the run with SST + 3 °C (b) and for the run with SST – 3 °C (c) compared to the reference run. Dots mark the measurement sites Corte (Co), Pont génois (Pg), Casaperta (Ca), Aléria (Al) and San Giuliano (SG) (see Figure 1).

4.2.2 Variability of the ABL depth along the Tavignano Valley and its reasons

As discussed in Section 2.2, the z_{BRN} reflects both the impact of surface- and upper layer-based processes on the ABL growth. In Figure 11, the spatial distribution of z_{BRN} is plotted together with the simulated kinematic heat flux, $H/(\rho\, c_p)$, the friction velocity, u_*, and the near-surface wind vectors for the upper part of the Tavignano Valley at 1100 UTC. The z_{BRN} values ≥ 1000 m AGL in the area of Corte and around 42.25° N, 9.2° E were correlated with higher kinematic sensible heat fluxes ($H/(\rho\, c_p) \approx 0.1$–$0.2$ K m s^{-1}) and higher friction velocities ($u_* \approx 0.4$–0.5 m s^{-1}) (Figure 11a, b). Between these two areas (around 42.29° N, 9.21° E), z_{BRN} values ≤ 500 m AGL are associated with lower $H/(\rho\, c_p)$ and lower u_* values. In the area around Pont génois, z_{BRN} is moderately high (≈ 500 m AGL south and 700 m AGL north of Pont génois) and $\sigma_{z_{BRN}}$ is quite high around noontime ($\sigma_{z_{BRN}} \approx 100$ m, Figure 9a), so that $\sigma_{z_{BRN}}$ reaches up to about 20 % of $\overline{z_{BRN}}$. However, here the $H/(\rho\, c_p)$ values are quite low (Figure 11a), while u_* values are high ($u_* \approx 0.4$–0.6 m s^{-1}, Figure 11b). That means, in the area around Corte and southeast of it a moderate degree of correlation between z_{BRN} and $H/(\rho\, c_p)$ respectively u_* is found, while in the area around Pont génois z_{BRN} cannot be explained by surface-based buoyancy-driven processes. Here, shear-driven mixing connected with the mountain wave must be mainly responsible for the spatial distribution of z_{BRN}.

The rapid increase of ABL depth at Corte was explained in Section 4.1. Abrupt increases and high ABL depths also occurred at Pont génois shortly after 0900 UTC and at Casaperta around 1100 UTC (Figures 9a and 10a). To investigate this, additional information of the vertical distribution of the mean and turbulent conditions in the valley atmosphere were taken into account.

Figure 12 shows the temporal evolution of profiles at Pont génois and Casaperta. The first considerable rise of z_{BRN} at Pont génois was shortly after 0900 UTC, i.e. when the stable ABL was eroded and the mountain wave accompanied by strong wind speed and wind shear and

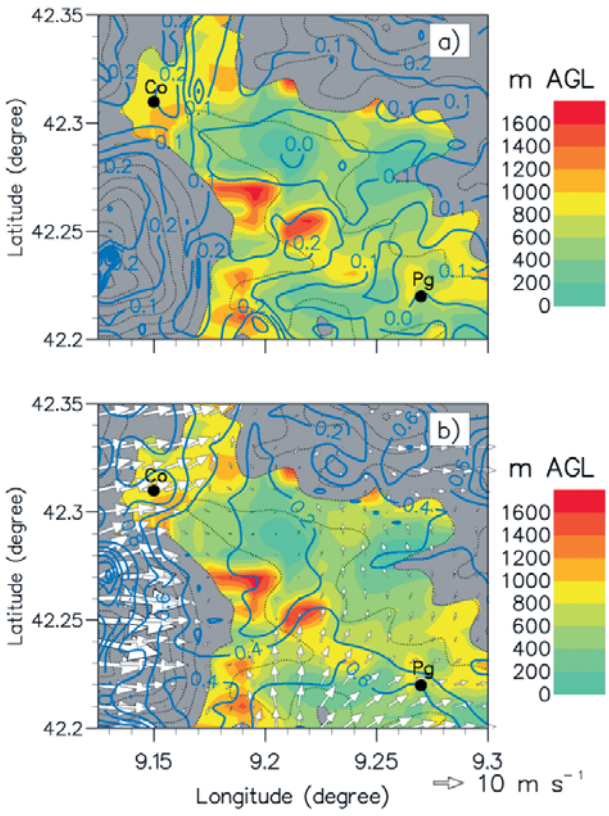

Figure 11: Simulated spatial distribution of z_{BRN} (colour-coded) in the upper part of the Tavignano Valley (terrain heights < 600 m MSL), terrain height (dotted black isolines) and kinematic surface sensible heat flux, $H/(\rho c_p)$, (in K m s^{-1}, blue isolines) (a), and ABL depth (colour-coded), terrain heights (dotted black isolines), friction velocity, u_* (in m s^{-1}, blue isolines) and horizontal wind at 10 m AGL (arrows) (b) at 1100 UTC. Dots mark the measurement sites Corte (Co) and Pont génois (Pg) (see Figure 1).

dry air penetrated down to the ground (Figure 12a, b). This behaviour is comparable to the one found at Corte (Figure 6). Strong mountain-wave generated wind and turbulence prevailed from 0900 to 1300 UTC (Figure 12a). The great spatial variability of z_{BRN} in the surrounding of Pont génois (Figures 9a and 10a) is affected by the position of the mountain wave. Depending on how strongly the area is influenced by the wave the threshold of $BRN = 0.22$ was reached at a lower or higher level and z_{BRN} varied between some hundred meters directly at Pont génois and about 1000 m AGL somewhat further north of Pont génois (Figure 11).

In contrast to the quite abrupt rises of z_{BRN} in Pont génois and Corte in the morning, z_{BRN} in Casaperta grew quite steadily by about 600 m between 0700 and 1000 UTC (Figure 12c). This growth rate is typical for an ABL driven by buoyancy and fits to the growth rate resulting from a high kinematic sensible heat flux (second term on the right-hand side of Eq. (2.2)). Observed and simulated relatively low *TKE* values at the surface and in the ABL during this period (Figures 4 and 12c) also indicate the absence of mountain-wave generated shear-driven turbulent mixing. The strong rise of z_{BRN} by several 100 m and subsequent fall between 1000 and 1200 UTC can be interpreted based on Figure 12c, d. Shortly before 1100 UTC the sea breeze with moist and cool air arrived at Casaperta resulting in a convergent flow accompanied with upward motion. That means, upward motion and high *TKE* values, present in the simulations up to about 1400 m MSL, caused a correspondingly deep ABL in which heat and moisture were well mixed. When the sea-breeze front had passed Casaperta, the z_{BRN} decreased rapidly, due to horizontal advection processes (fourth term on the right-hand side of Eq. (2.2)) and settled to values of $z_{BRN} \approx 300$ m AGL ($\hat{=}$ 350 m MSL), a typical value of the depth of the sea-breeze layer on this day (Figure 9). A similar behaviour – but less pronounced – was visible when the sea breeze arrived in Pont génois at about 1300 UTC (onset of phase III at Pont génois, see Section 4.1). The sea-breeze arrival was associated with a short increase of z_{BRN} and upward motion shortly after 1300 UTC (Figure 12a). Directly after the passage of the sea-breeze front, z_{BRN} decreased again reaching values of $z_{BRN} \approx 300$ m AGL ($\hat{=}$ 500 m MSL) at 1400 UTC.

4.2.3 Sea surface temperature modifications

The sea breeze and its inland propagation and hence, the ABL conditions are expected to depend on the SST. Therefore, the sensitivity of the ABL evolution with respect to SST changes was tested, modifying the SST by ±3 °C compared to the reference run (SST(modified) = SST(reference) ± 3 °C). The corresponding temporal behaviour of z_{BRN} for Corte is given in Figure 13. In both cases no significant differences can be found with respect to the transition from phase I to phase II, i.e. z_{BRN} rose strongly and abruptly after the erosion of the stable ABL. However, in case with a lower SST value, the sea breeze already arrived at Corte about 0.5 hours earlier, i.e. z_{BRN} dropped down earlier accompanied by a change to easterly winds and an increase of humidity (not shown). In case of the higher SST value the sea breeze was delayed by more than one hour. In all simulations, a stable ABL started to form at about 1630 UTC, including a shallow shear-driven ABL in its lower part ($z_{BRN} < 50$ m AGL, Figures 6 and 13).

The simulated spatial distributions of the ABL depth at 1100 UTC for both sensitivity experiments are shown in Figure 10b, c. It reveals that under conditions with a 3 °C lower SST, the ABL depth was lower in a broader section along the coastline and the lower part of the valley (Figure 10c) than in the reference run (Figure 10a). This is because the sea breeze had penetrated further inland at this time due to the larger horizontal temperature gradient resulting from the lower SST. The opposite holds for an SST by 3 °C higher than in the reference run (Figure 10b). Especially in the lower part of the valley, e.g. around Casaperta, strong differences of z_{BRN} compared to the reference run exist. At Casaperta, z_{BRN} values were higher as the sea breeze with its low ABL depth had not penetrated as far inland as in the reference run at 1100 UTC.

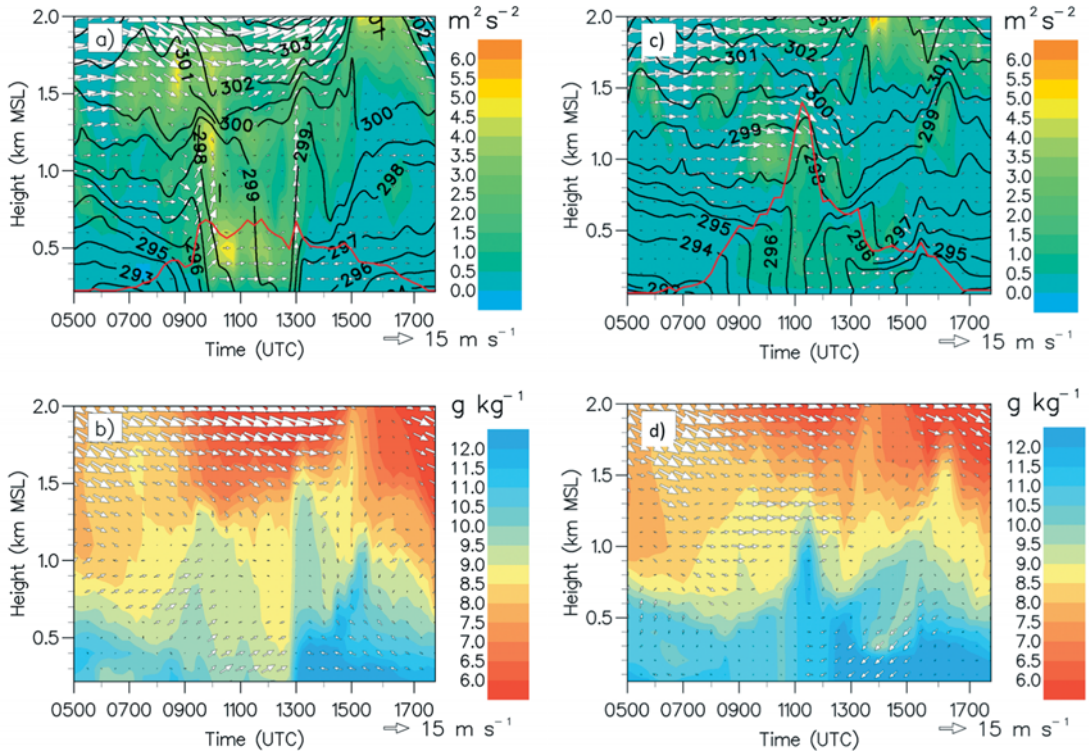

Figure 12: Simulated Θ (isolines), *TKE* (colour coded), u,w-wind vector (arrows, w component multiplied by a factor of 3) and z_{BRN} (solid red line) at Pont génois (a) and Casaperta (c) as well as specific humidity (colour coded) and u,v-wind vector (arrows) at Pont génois (b) and Casaperta (d).

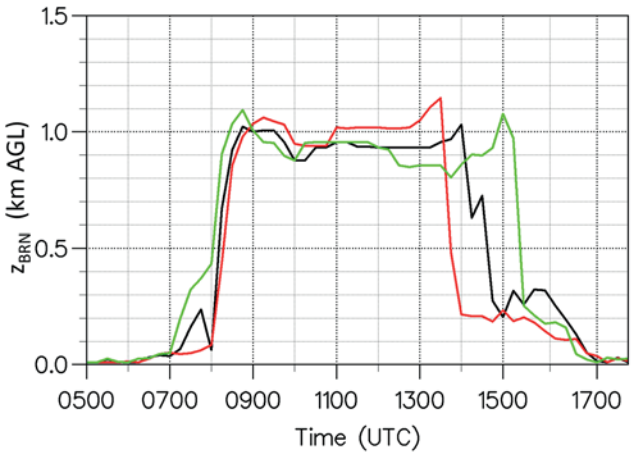

Figure 13: Simulated ABL depth z_{BRN} at Corte for the reference run (black) and the runs with SST − 3 °C (red) and SST + 3 °C (green) compared to the reference run.

5 Summary and conclusions

During the HyMeX campaign in 2012 intensive measurements were conducted on the mountainous island of Corsica. On 09 October, a large variability in ABL characteristics in the Tavignano Valley was observed. Based on the observational evidence, Adler and Kalthoff (2016) formulated hypotheses for the involved processes. In this study, high-resolution model simulations (500 m grid spacing) were performed with the COSMO model to close observational gaps and to allow for a model and observation-based understanding of the processes which were responsible for the spatio-temporal ABL variability. The main results from the combined model- and observation-based analyses are:

1. The model simulations prove that the mountain wave caused the abrupt change of the ABL conditions (wind speed and direction, humidity, TKE, ABL depth) at some sites in the upper part of the valley downwind of Corsica's main mountain crest, e.g. at Corte and Pont génois, after the stable ABL was eroded in the morning. Both, buoyancy- and shear-driven turbulence generated near the surface and mountain-wave generated shear-driven turbulence were responsible for the rapid dissolution of the stable ABL. The simulation could also explain why these changes occurred nearly at the same time at different sites in the upper part of the valley (Corte and Pont génois). The main reason was that these sites were at a similar position relative to the orientation of the mountain crest and, thus, relative to the axis of the mountain wave. The model simulations confirm that the strong and persistent downward motion at Corte during daytime was caused by the downward directed branch of the mountain wave. Additionally, the simulations verify the assumption that the upvalley propagating sea breeze caused the end of the period when ABL conditions were dominated by the mountain wave. Its arrival led to stabilisation of the valley atmosphere and a strong upward motion

in the afternoon due to horizontal wind convergence between the westerly wind in the subsiding branch of the mountain wave and the easterly flow in the sea breeze. Simultaneously, the mountain wave lifted off and retreated toward the western slope of the valley. By this, the layers above the ABL came under the influence of the ascending branch of the mountain wave, which explains the observed upward motion above the ABL.

2. The observations showed that the ABL conditions and depths differed considerably, both in space and time. The temporal changes could be quite abrupt, like the ones measured at Corte in the morning and at the different sites of the valley in the afternoon. The model reproduced the spatio-temporal variability of the ABL distribution and evolution in the valley. The simulation showed that the variability could even exist on a quite small scale (meso-γ scale). This spatial variability is more pronounced in the upper part of the valley than near the coast. That means, the individual sites are not necessarily representative for the ABL conditions of their surrounding, in particular in complex terrain when multi-scale processes affect the ABL.

3. The ABL conditions in the valley and at the coast depended on the SST, as the SST influenced the propagation speed of the sea-breeze front. The sea breeze reached the head of the valley about 0.5 hours earlier when the SST was by 3 °C lower than in the reference run. If the SST was by 3 °C higher than in the reference run, the sea breeze was delayed by more than one hour.

This study well demonstrates how observations and high-resolution simulations can be used together to gain more in-depth insight into atmospheric processes. Our findings emphasise the multi-scale interactions of processes and the small-scale variability of atmospheric fields over mountainous terrain. For a numerical model to be able to correctly simulate the ABL conditions in a valley it has to capture the involved scales and correctly reproduce the processes—with grid spacings of few kilometres in operational weather prediction models this is currently still beyond reach. The large sensitivity of the results to SST changes imposes an additional challenge for numerical weather prediction.

Acknowledgments

This work is a contribution to the HyMeX programme. We would like to thank Veronique Ducrocq from METEO-FRANCE and Evelyne Richard and Dominique Lambert from the University of Toulouse/CNRS for their support in performing the measurements of KITcube on the island of Corsica during HyMeX. We are grateful to the whole IMK team for deploying and running the KITcube on the island of Corsica and would like to thank Miriam Bentke for plotting some of the figures.

References

Adler, B., 2014: Boundary-layer processes producing mesoscale water-vapour variability over a mountainous island. – KIT Scientific Publishing, Karlsruhe, 242.

Adler, B., N. Kalthoff, 2014: Multi-scale transport processes observed in the boundary layer over a mountainous island. – Bound.-Layer Meteor. **153**, 515–537, DOI: 10.1007/s10546-014-9957-8.

Adler, B., N. Kalthoff, 2016: The impact of upstream flow on the atmospheric boundary layer in a valley on a mountainous island. – Bound.-Layer Meteor. **158**, 429–452, DOI: 10.1007/s10546-015-0092-y.

Adler, B., N. Kalthoff, M. Kohler, J. Handwerker, A. Wieser, U. Corsmeier, C. Kottmeier, D. Lambert, O. Bock, 2016: The variability of water vapour and preconvective conditions over the mountainous island of Corsica. – Quart. J. Roy. Meteor. Soc. **142**, 335–346, DOI: 10.1002/qj.2545.

Adler, B., N. Kalthoff, L. Gantner, 2017: Nocturnal low-level clouds over southern west africa analysed using high-resolution simulations. – Atmos. Chem. Phys. **17**, 899–910, DOI: 10.5194/acp-17-899-2017.

Atkinson, B.W., 1981: Meso-scale atmospheric circulations. – Academic Press, London, 495.

Barthlott, C., C. Hoose, 2015: Spatial and temporal variability of clouds and precipitation over Germany: multiscale simulations across the "gray zone". – Atmos. Chem. Phys. **15**, 12361–12384, DOI: 10.5194/acp-15-12361-2015.

Bischoff-Gauss, I., N. Kalthoff, S. Khodayar, M. Fiebig-Wittmaack, S. Montecinos, 2008: Model simulations of the boundary-layer evolution over an arid Andes valley. – Bound.-Layer Meteor. **128**, 357–379, DOI: 10.1007/s10546-008-9293-y.

Chow, F.K., A.P. Weigel, R.L. Street, M.W. Rotach, M. Xue, 2006: High-resolution large-eddy simulations of flow in a steep Alpine valley. Part i: Methodology, verification, and sensitivity experiments. – J. Appl. Meteor. Climatol. **45**, 63–86, DOI: 10.1175/JAM2322.1.

Coen, M.C., C. Praz, A. Haefele, D. Ruffieux, P. Kaufmann, B. Calpini, 2014: Determination and climatology of the planetary boundary layer height above the Swiss plateau by in situ and remote sensing measurements as well as by the COSMO-2 model. – Atmos. Chem. Phys. **14**, 13205–13221, DOI: 10.5194/acp-14-13205-2014.

De Wekker, S.F.J., M. Kossmann, 2015: Convective boundary layer heights over mountainous terrain – a review of concepts. – Front. Earth Sci. **3**, 77, DOI: 10.3389/feart.2015.00077.

Deardorff, J.W., 1972: Parameterization of the planetary boundary layer for use in general circulation models. – Mon. Wea. Rev. **100**, 93–106, DOI: 10.1175/1520-0493(1972)100<0093:POTPBL>2.3.CO;2.

Deardorff, J.W., 1974: Three-dimensional numerical study of the height and mean structure of a heated planetary boundary layer. – Bound.-Layer Meteor. **7**, 81–106, DOI: 10.1007/BF00227913.

Dipankar, A., B. Stevens, R. Heinze, C. Moseley, G. Zängl, M. Giorgetta, S. Brdar, 2015: Large eddy simulation using the general circulation model ICON. – J. Adv. Model. Earth Syst. **7**, 963–986, DOI: 10.1002/2015MS000431.

Driedonks, A., 1982: Models and observations of the growth of the atmospheric boundary layer. – Bound.-Layer Meteor. **23**, 283–306, DOI: 10.1007/BF00121117.

Drobinski, P., V. Ducrocq, P. Alpert, E. Anagnostou, K. Béranger, M. Borga, I. Braud, A. Chanzy, S. Davolio, G. Delrieu, others, 2014: Hymex: A 10-year mul-

tidisciplinary program on the Mediterranean water cycle. – Bull. Amer. Meteor. Soc. **95**, 1063–1082, DOI: 10.1175/BAMS-D-12-00242.1.

Ducrocq, V., I. Braud, S. Davolio, R. Ferretti, C. Flamant, A. Jansa, N. Kalthoff, E. Richard, I. Taupier-Letage, P.A. Ayral, others, 2014: HyMeX-SOP1: The field campaign dedicated to heavy precipitation and flash flooding in the northwestern Mediterranean. – Bull. Amer. Meteor. Soc. **95**, 1083–1100, DOI: 10.1175/BAMS-D-12-00244.1.

Duine, G.J., S.F. De Wekker, 2017: The effects of horizontal grid spacing on simulated daytime boundary layer depths in an area of complex terrain in Utah. – Env. Fluid Mech. 1–19, published online, DOI: 10.1007/s10652-017-9547-7.

Durran, D., 2015: Lee waves and mountain waves. – In: North G.R., J. Pyle, F. Zhang (Eds.): Encyclopedia of Atmospheric Sciences. – Academic Press, Oxford, second edition, 95–102.

Emeis, S., K. Schäfer, C. Münkel, 2008: Surface-based remote sensing of the mixing-layer height – a review. – Meteorol. Z. **17**, 621–630, DOI: DOI:10.1127/0941-2948/2008/0312.

Gantner, L., V. Maurer, N. Kalthoff, O. Kiseleva, 2017: The impact of land-surface parameter properties and resolution on the simulated cloud-topped atmospheric boundary layer. – Bound.-Layer Meteor. **165**, 475–496, DOI: 10.1007/s10546-017-0286-6.

Garratt, J.R., 1994: The atmospheric boundary layer. Cambridge Atmospheric and Space Science Series. – Cambridge University Press, Cambridge, 316.

Goger, B., M.W. Rotach, A. Gohm, O. Fuhrer, I. Stiperski, A.A. Holtslag, 2018: The impact of three-dimensional effects on the simulation of turbulence kinetic energy in a major alpine valley. – Bound.-Layer Meteor. **168**, 1–27, DOI: 10.1007/s10546-018-0341-y.

Goger, B., M.W. Rotach, A. Gohm, I. Stiperski, O. Fuhrer, G. De Morsier, 2019: A new horizontal length scale for a three-dimensional turbulence parameterization in mesoscale atmospheric modeling over highly complex terrain. – J. Appl. Meteor. Climatol. **58**, 2087–2102, DOI: 10.1175/JAMC-D-18-0328.1.

Haid, M., A. Gohm, L. Umek, H.C. Ward, T. Muschinski, L. Lehner, M.W. Rotach, 2020: Foehn-cold pool interactions in the Inn Valley during PIANO IOP2. – Quart. J. Roy. Meteor. Soc. **146**, 728, DOI: 10.1002/qj.3735.

Herzog, H.J., G. Vogel, U. Schubert, 2002: LLM – a nonhydrostatic model applied to high-resolving simulations of turbulent fluxes over heterogeneous terrain. – Theor. Appl. Climatol. **73**, 67–86, DOI: 10.1007/s00704-002-0694-4.

Honnert, R., 2016: Representation of the grey zone of turbulence in the atmospheric boundary layer. – Adv. Sci. Res. **13**, 63–67, DOI: 10.5194/asr-13-63-2016.

Jackson, P.L., G. Mayr, S. Vosper, 2013: Dynamically-driven winds. – In: Chow, F.K., S.F. De Wekker, B.J. Snyder (Eds.): Mountain weather research and forecasting, Springer Atmospheric Sciences, Springer, Dordrecht, 121–218, DOI: 10.1007/978-94-007-4098-3_3.

Jiang, Q., J.D. Doyle, 2008: Diurnal variation of downslope winds in Owens Valley during the Sierra Rotor Experiment. – Mon. Wea. Rev. **136**, 3760–3780, DOI: 10.1175/2008MWR2469.1.

Kalthoff, N., H.J. Binder, M. Kossmann, R. Vögtlin, U. Corsmeier, F. Fiedler, H. Schlager, 1998: Temporal evolution and spatial variation of the boundary layer over complex terrain. – Atmos. Env. **32**, 1179–1194, DOI: 10.1016/S1352-2310(97)00193-3.

Kalthoff, N., K. Träumner, B. Adler, S. Späth, A. Behrendt, A. Wieser, J. Handwerker, F. Madonna, V. Wulfmeyer, 2013: Dry and moist convection in the boundary layer over the Black Forest – a combined analysis of in situ and remote sensing data. – Meteorol. Z. **22**, 445–461, DOI: 10.1127/0941-2948/2013/0417.

Khodayar, S., N. Kalthoff, M. Fiebig-Wittmaack, M. Kohler, 2008: Evolution of the atmospheric boundary-layer structure of an arid Andes valley. – Meteor. Atmos. Phys. **99**, 181–198, DOI: 10.1007/s00703-007-0274-3.

Kirshbaum, D., B. Adler, N. Kalthoff, C. Barthlott, S. Serafin, 2018: Moist orographic convection: Physical mechanisms and links to surface-exchange processes. – Atmosphere **9**, 80, DOI: 10.3390/atmos9030080.

Kossmann, M., R. Vögtlin, U. Corsmeier, B. Vogel, F. Fiedler, H.J. Binder, N. Kalthoff, F. Beyrich, 1998: Aspects of the convective boundary layer structure over complex terrain. – Atmos. Env. **32**, 1323 – 1348, DOI: 10.1016/S1352-2310(97)00271-9.

Kossmann, M., U. Corsmeier, S.F.J. De Wekker, F. Fiedler, R. Vögtlin, N. Kalthoff, H. Güsten, B. Neininger, 1999: Observations of handover processes between the atmospheric boundary layer and the free troposphere over mountainous terrain. – Contr. Atmos. Phys. **72**, 329–350.

Lambert, D., M. Mallet, V. Ducrocq, F. Dulac, F. Gheusi, N. Kalthoff, 2011: CORSiCA: a Mediterranean atmospheric and oceanographic observatory in Corsica within the framework of HyMeX and ChArMEx. – Adv. Geosci. **26**, 125–131, DOI: 10.5194/adgeo-26-125-2011.

Lehner, M., M.W. Rotach, 2018: Current challenges in understanding and predicting transport and exchange in the atmosphere over mountainous terrain. – Atmosphere **9**, 276, DOI: 10.3390/atmos9070276.

Mahrt, L., 1981: Modelling the depth of the stable boundary-layer. – Bound.-Layer Meteor. **21**, 3–19, DOI: 10.1007/BF00119363.

Mayr, G.J., L. Armi, 2010: The influence of downstream diurnal heating on the descent of flow across the Sierras. – J. Appl. Meteor. Climatol. **49**, 1906–1912, DOI: 10.1175/2010JAMC2516.1.

Metzger, J., C. Barthlott, N. Kalthoff, 2014: Impact of upstream flow conditions on the initiation of moist convection over the island of Corsica. – Atmos. Res. **145**, 279–296, DOI: 10.1016/j.atmosres.2014.04.011.

Miltenberger, A., S. Pfahl, H. Wernli, 2013: An online trajectory module (version 1.0) for the nonhydrostatic numerical weather prediction model COSMO. – Geosci. Model Develop. **6**, 1989–2004, DOI: 10.5194/gmd-6-1989-2013.

Muñoz-Esparza, D., J.A. Sauer, R.R. Linn, B. Kosović, 2016: Limitations of one-dimensional mesoscale PBL parameterizations in reproducing mountain-wave flows. – J. Atmos. Sci. **73**, 2603–2614, DOI: 10.1175/JAS-D-15-0304.1.

Oke, T.R., 1992: Boundary layer climates, volume 5. – Psychology Press, 435.

Rampanelli, G., D. Zardi, 2004: A method to determine the capping inversion of the convective boundary layer. – J. Appl. Meteor. **43**, 925–933, DOI: 10.1175/1520-0450(2004)043<0925:AMTDTC>2.0.CO;2.

Raschendorfer, M., 2001: The new turbulence parameterization of LM. – In: COSMO newsletter, volume 1, 89–97, available at: http://www.cosmo-model.org/content/model/documentation/newsLetters/newsLetter01/newsLetter_01.pdf.

Rotach, M.W., D. Zardi, 2007: On the boundary-layer structure over highly complex terrain: Key findings from MAP. – Quart. J. Roy. Meteor. Soc. **133**, 937–948, DOI: 10.1002/qj.71.

Rotach, M.W., M. Andretta, P. Calanca, A.P. Weigel, A. Weiss, 2008: Boundary layer characteristics and turbulent exchange mechanisms in highly complex terrain. – Acta Geophys. **56**, 194–219, DOI: 10.2478/s11600-007-0043-1.

Schättler, U., G. Doms, C. Schraff, 2008: A description of the nonhydrostatic regional COSMO-model part vii: user's guide. – Deutscher Wetterdienst Rep. COSMO-Model **4**, 142.

Schmugge, T.J., M.J. Abrams, A.B. Kahle, Y. Yamaguchi, H. Fujisada, 2003: Advanced spaceborne thermal emission and reflection radiometer (ASTER). – In: Remote Sensing for Agriculture, Ecosystems, and Hydrology IV, volume 4879, 1–13. International Society for Optics and Photonics, DOI: 10.1117/12.469693.

Seibert, P., F. Beyrich, S.E. Gryning, S. Joffre, A. Rasmussen, P. Tercier, 2000: Review and intercomparison of operational methods for the determination of the mixing height. – Atmos. Env. **34**, 1001–1027, DOI: 10.1016/S1352-2310(99)00349-0.

Seidel, D.J., Y. Zhang, A. Beljaars, J.C. Golaz, A.R. Jacobson, B. Medeiros, 2012: Climatology of the planetary boundary layer over the continental United States and Europe. – J. Geophys. Res. **117**, D17106, DOI: 10.1029/2012JD018143.

Serafin, S., L. Strauss, V. Grubišić, 2017: Climatology of westerly wind events in the lee of the Sierra Nevada. – J. Appl. Meteor. Climatol. **56**, 1003–1023, DOI: 10.1175/JAMC-D-16-0244.1.

Serafin, S., B. Adler, J. Cuxart, S. De Wekker, A. Gohm, B. Grisogono, N. Kalthoff, D. Kirshbaum, M. Rotach, J. Schmidli, others, 2018: Exchange processes in the atmospheric boundary layer over mountainous terrain. – Atmosphere **9**, 102, DOI: 10.3390/atmos9030102.

Smith, R., 2015: Hydraulic flow. – In: G.R. North, J. Pyle, and F. Zhang (Eds.), Encyclopedia of Atmospheric Sciences, Academic Press, Oxford, second edition, 332–333, DOI: 10.1016/B978-0-12-382225-3.00165-1.

Sørensen, J., A. Rasmussen, H. Svensmark, 1996: Forecast of atmospheric boundary-layer height utilised for ETEX real-time dispersion modelling. – Phys. Chem. Earth **21**, 435–439, DOI: 10.1016/S0079-1946(97)81138-X.

Steyn, D., T. Oke, 1982: The depth of the daytime mixed layer at two coastal sites: A model and its validation. – Bound.-Layer Meteor. **24**, 161–180, DOI: 10.1007/BF00121666.

Steyn, D.G., S.F.J. De Wekker, M. Kossmann, A. Martilli, 2013: Boundary layers and air quality in mountainous terrain. – In: Chow, F.K., S.F.J. De Wekker, B.J. Snyder (Eds.): Mountain weather research and forecasting. – Springer Atmospheric Sciences, Springer, Dordrecht, 261–289, DOI: 10.1007/978-94-007-4098-3_5.

Strauss, L., S. Serafin, V. Grubišić, 2016: Atmospheric rotors and severe turbulence in a long deep valley. – J. Atmos. Sci. **73**, 1481–1506, DOI: 10.1175/JAS-D-15-0192.1.

Stull, R.B., 1988: An introduction to boundary layer meteorology. – Kluwer Academic Publishers, Dordrecht, 666.

Szintai, B., P. Kaufmann, 2008: TKE as a measure of turbulence. – In: COSMO Newsletter, volume 8, 2–10, available at: http://www.cosmo-model.org/content/model/documentation/newsLetters/newsLetter08/cnl8_szintai.pdf.

Vogelezang, D., A. Holtslag, 1996: Evaluation and model impacts of alternative boundary-layer height formulations. – Bound.-Layer Meteor. **81**, 245–269, DOI: 10.1007/BF02430331.

Vosper, S.B., 2004: Inversion effects on mountain lee waves. – Quart. J. Roy. Meteor. Soc. **130**, 1723–1748, DOI: 10.1256/qj.03.63.

Wetzel, P.J., 1982: Toward parameterization of the stable boundary layer. – J. Appl. Meteor. **21**, 7–13, DOI: 10.1175/1520-0450(1982)021<0007:TPOTSB>2.0.CO;2.

Whiteman, C.D., 2000: Mountain meteorology fundamentals and applications. – Oxford University Press, New York, 355.

Whiteman, C.D., J.C. Doran, 1993: The relationship between overlying synoptic-scale flows and winds within a valley. – J. Appl. Meteor. **32**, 1669–1682, DOI: 10.1175/1520-0450(1993)032<1669:TRBOSS>2.0.CO;2.

Wyngaard, J.C., 2004: Toward numerical modeling in the "Terra Incognita". – J. Atmos. Sci. **61**, 1816–1826, DOI: 10.1175/1520-0469(2004)061<1816:TNMITT>2.0.CO;2.

Zhong, S., F.K. Chow, 2013: Meso-and fine-scale modeling over complex terrain: Parameterizations and applications. – In: Chow, K.W. S.F.J. De Wekker, B.J. Snyder (Eds.): Mountain Weather Research and Forecasting. – Springer, 591–653, DOI: 10.1007/978-94-007-4098-3_10.

Zhong, S., J. Doran, 1995: A modeling study of the effects of inhomogeneous surface fluxes on boundary-layer properties. – J. Atmos. Sci. **52**, 3129–3142, DOI: 10.1175/1520-0469(1995)052<3129:AMSOTE>2.0.CO;2.

Zhou, B., J.S. Simon, F.K. Chow, 2014: The convective boundary layer in the terra incognita. – J. Atmos. Sci. **71**, 2545–2563, DOI: 10.1175/JAS-D-13-0356.1.